

The Contraction/Expansion History of Charon with implication for its Planetary Scale Tectonic Belt

Uri Malamud, Hagai B. Perets and Gerald Schubert

September 8, 2018

uri.mal@tx.technion.ac.il

hperets@physics.technion.ac.il

schubert@ucla.edu

Department of Physics, Technion, Israel

Department of Earth, Planetary and Space Sciences, University of California, L.A

Abstract

The New-Horizons mission to the Kuiper Belt has recently revealed intriguing features on the surface of Charon, including a network of chasmata, cutting across or around a series of high topography features, conjoining to form a belt. It is proposed that this tectonic belt is a consequence of contraction/expansion episodes in the moon's evolution associated particularly with compaction, differentiation and geophysical reactions of the interior. The proposed scenario involves no need for solidification of a vast subsurface ocean and/or a warm initial state. This scenario is based on a new, detailed thermo-physical evolution model of Charon that includes multiple processes. According to the model, Charon experiences two contraction/expansion episodes in its history that may provide the proper environment for the formation of the tectonic belt. This outcome remains qualitatively the same even if we assume a different initial composition and mass. Two alternative explanations for the precise localization and orientation of Charon's tectonic belt are speculated.

1 Introduction

NASA's New-Horizons spacecraft has recently completed a close approach to the Pluto system. The initial observations reveal Charon to have intricate geological surface features that vary in scale, shape and orientation. Among the most notable set of features, is a network of NE-SW trending fractures that cut across most of the sub-Pluto hemisphere. Perhaps the most prominent and intriguing of these, is a structure named Serenity Chasma, a two-walled, several kilometers deep graben, and up to 60 km wide (Stern *et al.*, 2015). In addition, the chasmata network appears to cut through or around a series of high topography features, conjoining to form a belt, to which we will refer, for the remainder of this paper, as the *tectonic belt* (see the highlighted region in Figure 1). This belt seems to at least partially extend to the anti-Pluto hemisphere as well, suggesting that certain compressional/extensional processes have altered the surface of Charon on a global scale during some point or points in its evolution. Serenity Chasma in particular, seems to be highly indicative of an extensional environment. Several alternatives for triggering a global size increase can be suggested.



Figure 1: The tectonic belt marked in light blue. Credits: NASA/JHUAPL/SwRI

One possible explanation is the freezing of a global sub-surface water ocean (Rhoden *et al.*, 2015). Since the solid phase of water has a lower specific density than the liquid phase, the result would be an increase in volume. This, however, suffers from several difficulties. First, in order to account for the surface area increase that is implied by the width of Serentiy Chasma, the sub-surface ocean must be vast. According to our model (Section 3) a vast ocean never forms because of the relatively small size of Charon and the lack of short-lived radiogenic heating. Arguably, if a significant amount of energy is released as a result of tidal heating during the synchronization phase of Pluto and Charon, this conclusion could change. However, for significant tidal heating during synchronization, Charon is required to have experienced a transient high eccentricity phase as its orbit expanded (Rhoden *et al.*, 2015). While this is theoretically possible (Ward and Canup, 2006; Cheng *et al.*, 2014), the smaller size of Charon compared to Pluto makes it more likely that the tides raised by Pluto on Charon would damp Charon's eccentricity (Barr and Collins, 2015), leading to circularization.

Moreover, the same high eccentricity models that predict tidally-induced extensional fractures (as opposed to zero eccentricity orbital expansion with tidal bulge collapse only) require an ocean layer (Rhoden *et al.*, 2015). However, under regular assumptions (heating by long-lived radionuclides only), the time scale of Charon's circularization (up to several Myr) is much shorter than the time required to even produce liquid water (at least 100 Myr, see Section 3). Thus, in order to form tidally-induced and/or ocean freezing extensional fractures, one has to assume that a sufficient amount of heat was initially supplied in the process that led to Charon's formation. There are currently three alternative formation models for Charon: the giant impact model (Canup, 2005; Stern *et al.*, 2006), the dynamical capture model (Pires dos Santos *et al.*, 2012) and the in-situ formation model of the Pluto-Charon binary (Nesvorný *et al.*, 2010). None of these models can unequivocally provide the conditions necessary for the formation of an early ocean. According to Canup (2005), the case for early melting and differentiation of Charon in the giant impact model is perhaps possible, but far weaker for Charon, compared to

Pluto, given its size and the precise details concerning its formation. The analysis of Pires dos Santos *et al.* (2012) does not provide any detailed information regarding the initial state of Charon after a capture. In-situ formation is the least likely model to provide this amount of heat, and therefore it remains uncertain if any of these scenarios can produce the required early ocean.

Given these difficulties, the goal of this paper is therefore to explore an alternative model that has the potential to induce an extensional environment, without the need for a vast subsurface ocean, and without the necessity of a warm initial state. We also explain, by the same model, how Charon could display both extensional and compressional features in the same tectonic belt.

The paper is arranged as follows. In Section 2 we outline the thermo-physical evolution model used in order to calculate the evolution of Charon. In Section 3 model results are presented and they are discussed in Section 4. We conclude with a summary of our findings in Section 5.

2 The Model

The model used in this study is based on the model of Malamud and Prialnik (2015), which is an extension of earlier models by Prialnik and Merk (2008) and Malamud and Prialnik (2013). This code has been developed in order to study the evolving thermal and physical state of any moderate-sized icy object (large enough to be in hydrostatic equilibrium but not so large as to permit full or partial melting of the rock). It includes the following processes: (1) internal differentiation by the multiphase flow of water (2) compaction by self-gravity (3) geochemical reactions. In terms of energy sources, it considers nearly the entire energy budget, including: short and long lived radioactive nuclides, latent heat released/absorbed by geochemical reactions, surface insolation, gravitational energy associated with internal redistribution of mass and/or size change, and latent heat of crystallization of amorphous ice. The model treats heat transport by conduction and

advection (parameterized convection has not been included since Charon is most likely conductive, see also the analysis by Hussmann *et al.* (2006)). We follow the transitions among four phases of water (amorphous ice, crystalline ice, liquid and vapor), and two phases of silicates (aqueously altered rock and non-altered rock), accounting for thermal (conductivity, heat capacity) and physical (density) changes in the solid phases as the body evolves, undergoing heating by long-lived radionuclides primarily.

The predecessor model of Malamud and Prialnik (2015) has already been used to evaluate the evolution of three moderate-sized Kuiper Belt objects (KBOs) including Charon. Nevertheless, the model presented in this study has two improvements: (1) it considers serpentine dehydration, and (2) constant solar luminosity is not assumed. The former modification is very important. The previous model only included the process of serpentinization - which leads to energy release as well as rock density decrease and absorption of water in the rock. Now the inverse process, dehydration, is also considered - leading to energy absorption as well as rock density increase and water release. The addition of dehydration considerably changes the course of Charon's evolution, not only due to the rock's physical and thermal modification, and the considerable amounts of water released, but also, since dehydration is an endothermic process, acting as a powerful energy sink that suppresses Charon's peak temperatures. The derivation of the dehydration equations is presented in Malamud and Prialnik (2016). The second modification is a small one, but it offers some improvement compared with our previous studies, as well as most evolution models, which typically consider a constant solar luminosity in order to derive the object's surface boundary conditions. In fact, the solar luminosity is not constant. It was approximately 30% lower at the birth of the solar system and increased over time. Here we consider the change in solar luminosity as a function of time, as obtained by a 1-solar mass MESA stellar evolution (Paxton *et al.*, 2011).

2.1 Set of Equations

Considering the transitions between four different phases of water – amorphous ice, crystalline ice, liquid and vapor, and between two phases of silicates – aqueously unaltered and aqueously processed, we have six different components that we denote by subscripts: u - aqueously unaltered rock; p - aqueously processed rock; a - amorphous water ice; c - crystalline water ice; ℓ - liquid water; v - water vapor.

The independent variables are: the cumulative volume V ; temperature T ; densities ρ_a , $\rho_w = \rho_c + \rho_\ell$, ρ_v and ρ_d , as well as the mass fluxes J_v (water vapor) and J_ℓ (liquid water), as functions of 1-D space and time t . The set of equations to be solved is:

$$\frac{\partial(\rho U)}{\partial t} + \frac{\partial}{\partial V} \left(-K \frac{\partial T}{\partial V} \right) + \frac{\partial(U_v J_v + U_\ell J_\ell)}{\partial V} + q_\ell \mathcal{H}_\ell - S = 0 \quad (1)$$

$$\frac{\partial \rho_v}{\partial t} + \frac{\partial(J_v)}{\partial V} = q_v \quad (2)$$

$$\frac{\partial \rho_w}{\partial t} + \frac{\partial J_\ell}{\partial V} = \lambda(T) \rho_a - q_v + \frac{2A_w}{A_u} (R_D \rho_p - R_S \rho_u) \quad (3)$$

$$\frac{\partial \rho_a}{\partial t} = -\lambda(T) \rho_a \quad (4)$$

$$J_v = -\phi_v \frac{\partial (P_v / \sqrt{T})}{\partial V} \quad (5)$$

$$J_\ell = -\phi_\ell \left(\frac{\partial(P_\ell)}{\partial V} + \rho_\ell g \right) \quad (6)$$

$$Gm\rho = -4\pi(3/4\pi)^{4/3} V^{4/3} \frac{\partial P}{\partial V} \quad (7)$$

Equations (2-4) are the mass conservation equations, where $\lambda(T)$ is the rate of crystallization of amorphous ice, R_S is the serpentinization rate, R_D is the dehydration rate and q_v is the rate of sublimation/evaporation or deposition/condensation, respectively. The mass fluxes are given by eqs (5) and (6), where ϕ_v and ϕ_ℓ are the permeability coefficients.

In the energy conservation equation (1), U denotes energy per unit mass, \mathcal{H}_ℓ is the latent heat of fusion (melting), q_ℓ is the rate of melting/freezing, and K is the effective thermal conductivity, accounting for heat transferred by conduction/convection, while

$(U_v J_v + U_\ell J_\ell)$ accounts for the heat transferred by advection. The sum of all energy sources S includes the energy supplied by crystallization of amorphous ice, the energy lost by sublimation, and all the other possible internal heat sources, such as radiogenic heating, tidal heating, change in gravitational potential energy and heat released or absorbed by geochemical reactions. The last equation, eq. (7), imposes hydrostatic equilibrium, using the equation of state of Malamud and Prialnik (2015)), for the hydrostatic pressure P . All the other variables are easily derived from the independent variables and the volume distribution. The boundary conditions adopted here are straightforward: vanishing fluxes at the center and vanishing pressures at the surface. The surface heat flux is given by the balance between solar irradiation (albedo dependent), thermal emission and heat absorbed in surface sublimation of ice. We note that for an eccentric orbit, distance variations on the scale of the orbital period, would render the changes in the surface boundary condition extremely fast, and therefore the calculation extremely slow, as time steps are dynamically adjusted. For relatively small eccentricities one may circumvent this problem by considering an effective circular semi-major axis, producing an equivalent average insolation (Williams and Pollard, 2002). This technique is used here for the Pluto/Charon system (the effective correction is very small, despite a notable non-circular heliocentric orbit).

2.2 Numerical Scheme

The model uses an adaptive-grid technique, specifically tailored for objects that change in mass or volume. Since the body is allowed to grow or shrink (as a result of various internal processes), a moving, time dependent boundary condition is implemented. The numerical solution is obtained by replacing the non-linear partial differential equations with a fully implicit difference scheme and solving a two-boundary value problem by relaxation in an iterative process. Time steps are adjusted dynamically according to the number of iterations. The volume is distributed over a variable x that assumes integer values of i , from $i = 1$ at the center to $i = I$ at the surface; here we use $I = 100$.

Thus, an equation is required for determining the grid zoning, to be solved along with the others. Here we use a geometric series for volume distribution over the grid points. Since temporal derivatives are taken at constant V , whereas $V = V(x, t)$, the following transformation is implemented in the difference scheme:

$$\left(\frac{\partial}{\partial t}\right)_V = \left(\frac{\partial}{\partial t}\right)_x - \left(\frac{\partial V}{\partial t}\right)_x \cdot \left(\frac{\partial}{\partial V}\right)_t \quad (8)$$

3 Results of Evolutionary Calculation

3.1 Model configuration and parameters

We begin the evolution with a fully accreted object whose initial structure is homogeneous, with a well-mixed composition of rock and ice. This initial structure is the most basic to assume, since it requires no a-priori assumption of any specific formation mechanism which may lead to warm or otherwise heterogeneous accretion. By the same argument, we start with amorphous ice. Most of the important initial and physical parameters used in our model are listed in Table 1. We assume an initial rock fraction of 77% corresponding to the newest mass measurement (Brozović *et al.*, 2015), which yields a bulk density of 1.7 g cm^{-3} (Stern *et al.*, 2015), following a 4.6 Gyr evolution. Note that for completeness we also considered an initial rock fraction of 75% based on a previous mass estimate (Buie *et al.*, 2006). For both selections, however, the rock/ice mass ratio is compatible with a previous study (Malamud and Prrialnik, 2015), and the resulting internal structures and evolutionary paths are qualitatively indistinguishable. We therefore describe below only the results based on the newer mass estimate. The rock contains the long-lived radionuclides ^{235}U , ^{40}K , ^{238}U and ^{232}Th , with initial abundances typical of meteorites. Short-lived radionuclides can be neglected, since the accretion time of Charon is expected to be much longer than in the inner solar system (Kenyon and Bromley, 2012), on the order of tens of Myr. It remains to determine the surface boundary condition that will define the surface temperature. The surface boundary condition is determined by

the stellar irradiation, according to the distance from the Pluto-Charon system to the Sun. As previously mentioned, the insolation is not assumed to be constant throughout the evolution, since its time dependence is well established from stellar evolution models. The orbital parameters of the Pluto-Charon system on the contrary, are assumed to be constant and equal to the present day observed values, since the orbital history is harder to constrain.

Table 1: Initial and physical parameters

Parameter	Symbol	Value
Initial uniform temperature	T_0	70 K
Nominal ^{235}U abundance	$X_0(^{235}\text{U})$	$6.16 \cdot 10^{-9}$
Nominal ^{40}K abundance	$X_0(^{40}\text{K})$	$1.13 \cdot 10^{-6}$
Nominal ^{238}U abundance	$X_0(^{238}\text{U})$	$2.18 \cdot 10^{-8}$
Nominal ^{232}Th abundance	$X_0(^{232}\text{Th})$	$5.52 \cdot 10^{-8}$
Albedo	\mathcal{A}	0.38
Pluto-Charon semi-major axis	a	39.264 AU
Pluto-Charon eccentricity	e	0.24897
Ice specific density	$\rho_{a,c}$	0.917 g cm^{-3}
Water specific density	ρ_ℓ	0.997 g cm^{-3}
Rock specific density (u)	ρ_u	$3.5 + 2.15 \cdot 10^{-12}P \text{ g cm}^{-3}$
Rock specific density (p)	ρ_p	$2.9 + 3.41 \cdot 10^{-12}P \text{ g cm}^{-3}$
Water thermal conductivity	K_ℓ	$5.5 \cdot 10^4 \text{ erg cm}^{-1} \text{ s}^{-1} \text{ K}^{-1}$
Ice thermal conductivity (c)	K_c	$5.67 \cdot 10^7/T \text{ erg cm}^{-1} \text{ s}^{-1} \text{ K}^{-1}$
Ice thermal conductivity (a)	K_a	$2.348 \cdot 10^2 T + 2.82 \cdot 10^3 \text{ erg cm}^{-1} \text{ s}^{-1} \text{ K}^{-1}$
Rock thermal conductivity (u)	K_u	$10^5/(0.11 + 3.18 \cdot 10^{-4}T) + 3.1 \cdot 10^{-5}T^3 \text{ erg cm}^{-1} \text{ s}^{-1} \text{ K}^{-1}$
Rock thermal conductivity (p)	K_p	$10^5/(0.427 + 1.1 \cdot 10^{-4}T) + 8.5 \cdot 10^{-6}T^3 \text{ erg cm}^{-1} \text{ s}^{-1} \text{ K}^{-1}$

3.2 The evolutionary course

The course of the evolution is illustrated by a series of figures showing properties as a function of time and radial distance from the center of the body. Since the radius of Charon changes during evolution (eventually converging to 606 km), the upper boundary of the plots also changes with time. The evolution of Charon proceeds in several steps, corresponding to different processes in the interior:

Step 1 ($0 < t < 137$ Myr): In this time interval the temperatures are always below the melting point of water, as shown in Figure 2, so the only process that modifies the structure (and size) of Charon is compaction of the ice in the interior. As the ice gets warmer (from an initially cold 70 K) it becomes more susceptible to compaction, so the radius decreases.

Step 2 ($137 \text{ Myr} < t < 164 \text{ Myr}$): The melting temperature is reached. This drives rapid differentiation by liquid water flow, powered by rapid release of energy from serpentinization. In the process, the initially anhydrous rock becomes hydrated (Figure 3 shows the rock phase transitions), and a large fraction of the free water in the system is absorbed in the rock. The net effect of ice melting and incorporation in the rock is a further decrease in radius. A pristine outer layer, 35 km thick, of ice/rock mixture, keeps its original anhydrous rock, since it is too cold for liquid water to reach. About two thirds of this layer (23 km) is too cold even for vapor transport, thus it retains the initial rock/ice ratio. The outermost 10 km is so cold, that it retains amorphous ice; elsewhere the ice crystallizes (See Figure 4). Directly beneath the pristine outer layer, there is a transition layer, from fully anhydrous rock (a relative mass fraction of 1) to fully serpentinized rock (a relative mass fraction of 0), some 25 km thick. Combined, these two layers are 60 km thick. All underlying mantle silicates are fully hydrous. Note the energetic significance of serpentinization, without which these outer layers could be much thicker (the massive amount of energy released by serpentinization, generates higher temperatures further out toward the surface).

Step 3 ($164 \text{ Myr} < t < 450 \text{ Myr}$): Differentiation continues, since there is still free

water (liquid) in the interior. The already hydrated rock can no longer absorb any free water, so that all remaining water is transported to the coldest regions and begins to freeze at the base of the mantle (Figure 5), constantly thickening it, until there is essentially no longer free water in the interior by 450 Myr. At this point the ice-rich mantle is about 120 km thick, and it remains approximately (but not exactly) that size throughout the rest of the evolution. The remaining rocky core is still relatively porous at this stage (see the porosity distribution in Figure 6 where porosity is defined as the volume fraction not occupied by solid or liquid phases), given the size of Charon, and the (still) cold core temperatures, which do not enhance rock compaction. In the absence of core compaction, the freezing of ice at the base of the mantle results in an expansion in volume, so the outcome of this stage is an increase in size. Note that the size increase is exponential, so that most of it already occurs by 300 Myr. The core temperature continues to increase as a result of radiogenic heating.

Step 4 ($450 \text{ Myr} < t < 1 \text{ Gyr}$): After about 450 Myr, the temperature in the interior warms to above 450 K. This is when the rock starts to be a little more susceptible to compaction - a tendency which keeps increasing with temperature (given our compaction EOS). When core compaction is triggered, the expansion stops and the radius of Charon begins to decrease as a result of core compaction by self-gravity.

Step 5 ($1 \text{ Gyr} < t < 4.6 \text{ Gyr}$): After 1 Gyr, the temperature in the core reaches approximately 675 K, at which point the reverse process to serpentinization starts increasing in rate, the rock rapidly exuding the water it had absorbed. The central part of the body becomes dehydrated, so now the stratification is more complex: an anhydrous rocky core, underlying an outer, colder, hydrous rocky layer (see Figure 3). Dehydration also acts as a powerful internal energy sink, suppressing (but not counteracting) the increase of temperatures by radiogenic heating. As the evolution advances the inner core grows, with temperatures increasing outward. The released water migrates to the base of the mantle and freezes; so, by the end of the evolution (4.6 Gyr), the fraction of free water globally increases from 13.2% (that is, after serpentinization, during which about 10% of

the water becomes embedded in the hydrated rocks) to about 16.5%. This transition is depicted in terms of rock/ice mass ratio in Figure 7 – recalling that the initial rock/ice mass ratio was 3.33 (or 23 % water fraction). Meanwhile, increasing core temperatures act to reduce the core porosity, hence reducing Charon’s size. On the other hand, water freezing in at the base of the mantle has the inverse effect. The net result of the two competing effects is that first a significant decrease in radius occurs, and only after the interior begins to cool (approximately 2.25 Gyr), when the core porosity becomes fixed at its minimum, is there a radius increase, albeit a very small one.

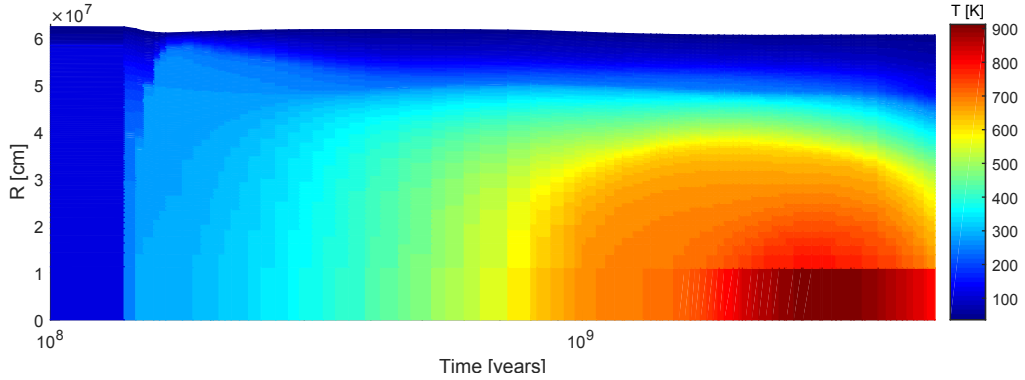


Figure 2: Temperature as a function of time and radial distance.

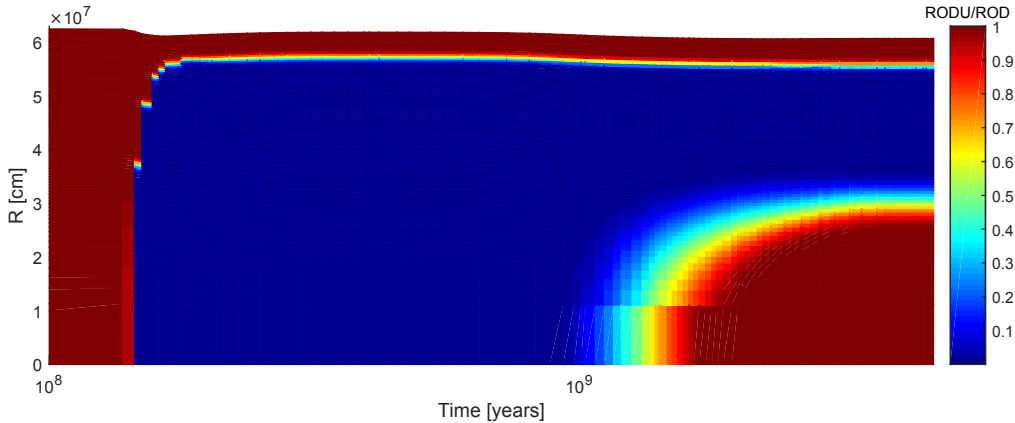


Figure 3: Anhydrous rock density to total rock (hydrous+anhydrous) density, as a function of time and radial distance.

The contribution of gravitational energy by compaction/expansion or internal re-distribution of mass is found to be negligible, as expected from all previous studies

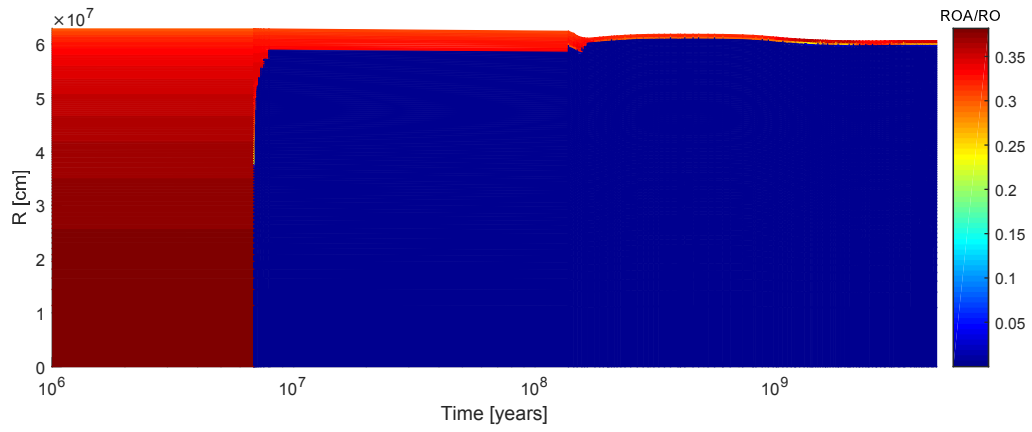


Figure 4: Amorphous ice density to total density, as a function of time and radial distance.

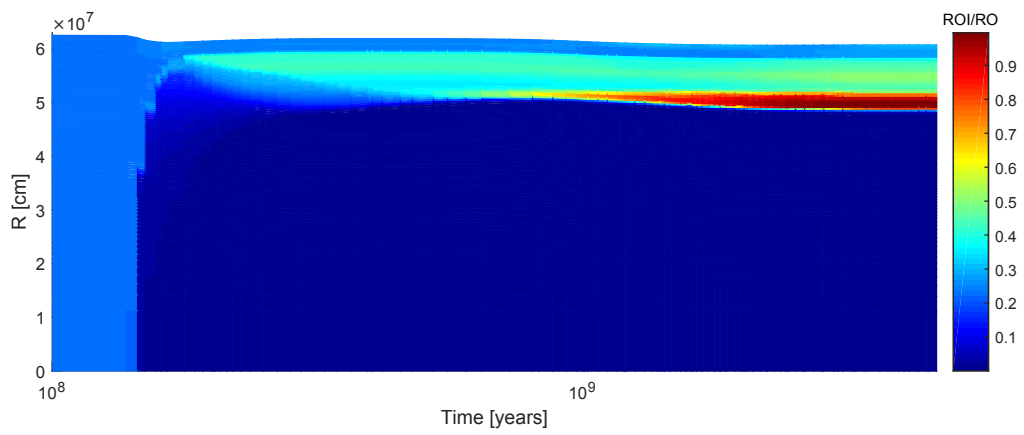


Figure 5: Ice density (crystalline + amorphous) to total density, as a function of time and radial distance.

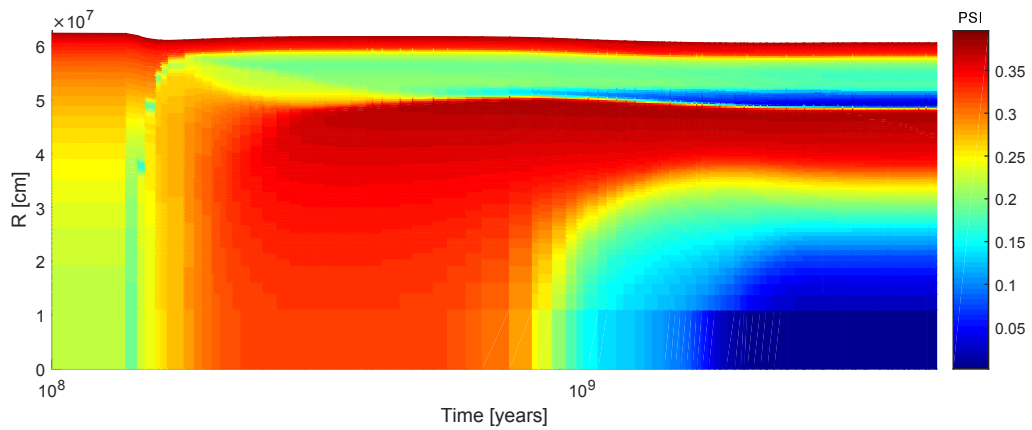


Figure 6: Porosity as a function of time and radial distance.

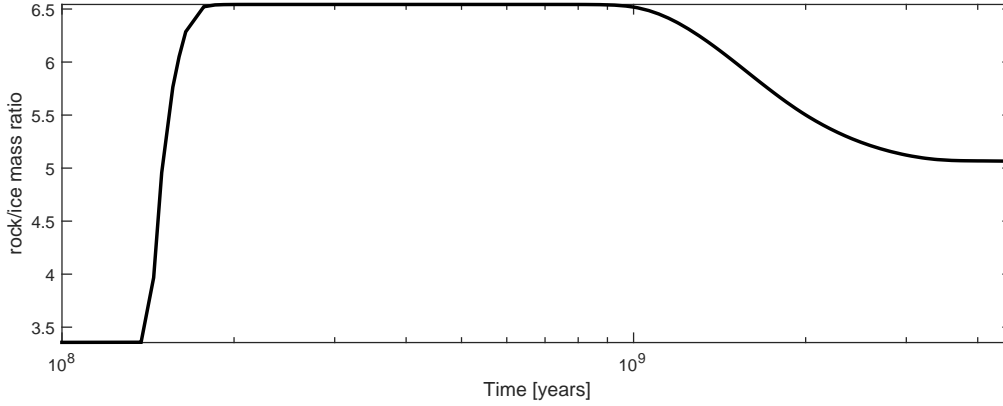


Figure 7: Global rock/ice mass ratio as a function of time.

(Desch *et al.*, 2009; Malamud and Prialnik, 2015). At any point in time the temperature decreases monotonically from the center of the body to the surface (Figure 2). The porosity, by contrast, has two distinct peaks during most of the evolution, one near the core boundary and another in the outermost layer of the object, as shown in Figure 6. At the center, where the temperature and pressure are highest, the porosity is almost vanishing, increasing toward the core boundary. The same trend is exhibited in the icy mantle, which is very compact at the bottom, where the temperature and pressure are highest, and the rock fraction is lowest, in contrast with the overlying surface layers. The total density (see Figure 8) decreases monotonically from the center of the body to the core-mantle boundary, at which point its profile becomes more complicated, with a local minimum at the base of the mantle, corresponding to the highest degree of ice enrichment (the density converges to that of pure, non-porous ice). This configuration is gravitationally unstable; however, for an overturn by Rayleigh-Taylor instability to occur, the viscosity has to be sufficiently low, and thus the temperature sufficiently high, for a suitable amount of time (Rubin *et al.*, 2014). We find that for the bulk of the evolution presented above, mantle conditions do not permit overturn by Rayleigh-Taylor instability. Finally, a schematic depiction of the present day structure and composition of Charon, according to the model, is shown in Figure 9.

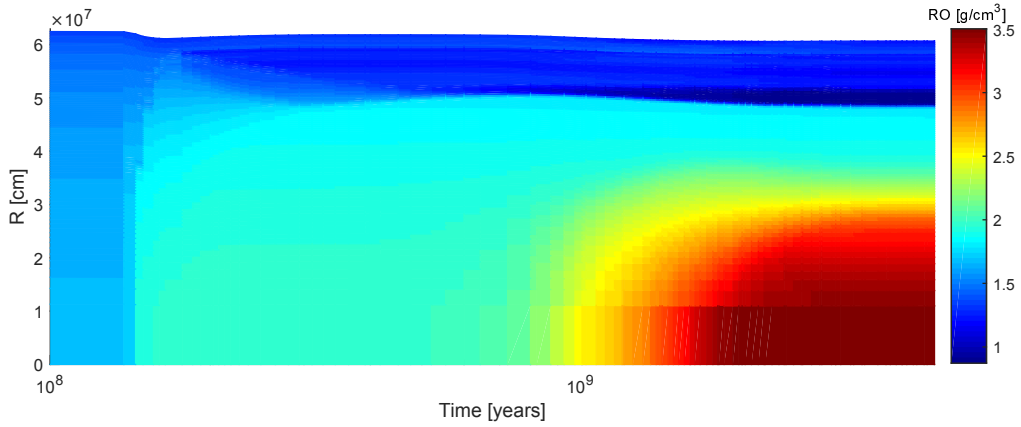


Figure 8: Total density as a function of time and radial distance.

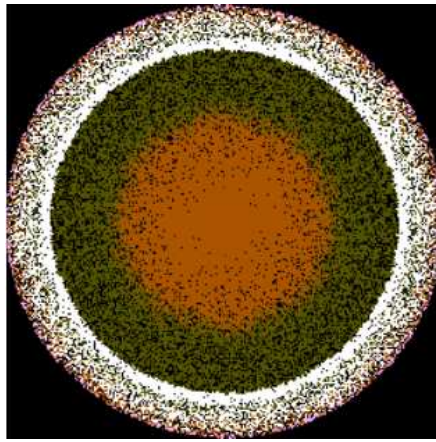


Figure 9: Present day cross-section - color interpretation: *black* (pores); *white* (crystalline ice); *pink* (amorphous ice); *brown* (anhydrous rock); and *olive* (hydrated rock)

4 Discussion

4.1 Present Day Structure Compared with Previous Models

We discuss and compare several models of Charon, focusing on its present day structure. The model presented above shows only one potential outcome of the long-term evolution of Charon, although the initial conditions and model parameters are judiciously chosen. It is important to point out, that given some changes in the parameter space (e.g., different grain specific densities, different thermal conductivities, inclusion of antifreeze to lower the water melting point, etc.), within reasonable constraints, the results still remain

qualitatively the same. The end structure obtained for Charon is always differentiated into a rocky core (approximately 485 km) and an ice-enriched mantle (approximately 120 km). The rocky core is further stratified into an inner dehydrated part (250 km) and outer hydrated part (135 km), separated by a transition layer (100 km). The ice-enriched mantle is more complex. It is composed of pure ice at its base, the rock fraction variably increasing toward the surface. The rock undergoes a transition from fully hydrated to fully dehydrated. The outermost coldest layer preserves the original anhydrous rock, as well as the original rock/ice ratio (and it contains yet a thinner surface layer that may preserve its amorphous ice). While the sizes given above may change for different choices of parameter space, the layout remains the same.

Other thermal evolution models have been used in order to study Charon's internal structure, reaching similar results in some instances, albeit using very different model assumptions. The model of Hussmann *et al.* (2006) considers the heat transport inside a zero-porosity object whose size is fixed and equals the present day observed size. Charon is assumed (not calculated) to have a 2-layered structure, an icy shell overlying a rocky core, each layer being homogeneous. It is shown to be conductive only. The core radius is 405 km, smaller than what we obtain when porosity is accounted for, although a direct comparison is inexact since their assumed size and bulk density are outdated.

The model of Desch *et al.* (2009) is more sophisticated, since it also calculates the differentiation of an initially well-mixed icy object, albeit in a simpler way, assuming that rock and water separate instantaneously upon passing a certain temperature threshold. Their evolution of Charon results in a differentiated structure of a rocky core (around 420 km), underlying a layer of ice, underlying an outer layer (of approximately 70 km) that preserves the original well-mixed rock/ice material (these values vary considerably for different parameter choices). The layers are homogeneous. In a later study, Rubin *et al.* (2014) lower the temperature threshold, considering the effect of crustal overturn by Rayleigh-Taylor instability, to obtain only a ~ 60 km outer layer, and a similarly larger rocky core (all other model parameters being equal). This configuration is somewhat

closer to the final configuration obtained by our model. However, their model assumes zero porosity and layers of homogeneous density. It also does not consider geochemical reactions, thereby disregarding the important physical and energetic contributions of these processes.

To our knowledge, the most detailed thermo-physical evolution model of Charon prior to this study, is that of Malamud and Prialnik (2015). Their model explicitly considers the multiphase flow and migration of water inside a porous medium, including compaction by self-gravity, and thus follows the differentiation of Charon in greater detail. It further considers serpentinization, the transition from initially anhydrous rock to hydrous rock, accounting for the water embedded in the rock and the consequent energy release. This energy elevates the near surface temperatures, so that liquid water can reach considerably closer to the surface, altering the structure of the mantle. Their model does not however consider serpentine dehydration, which changes the physical and thermal properties of the inner rocky core, releases water back to the system, and lowers the peak core temperatures. These, as well as additional smaller modifications have been added in this study. The result is a more detailed and more complete model. Although a direct comparison to previous studies is difficult, given variations in the parameter space, we summarize in Table 2 some characteristic results from all 4 studies discussed above, accentuating the qualitative differences in the present day structure.

The most noticeable trends, apart from increasing structural complexity with each evolution model, is (1) the larger core size, and (2) lower peak temperatures. The increase in core size is a natural outcome when accounting for non-negligible porosity and geochemical reactions, although Desch *et al.* (2009) and Rubin *et al.* (2014) have in some cases lowered the homogeneous core density to only 2.35 g cm^{-3} , which may be seen as equivalent to adding constant porosity. Different peak temperatures are probably a result of different choices for the thermal conductivity coefficients, as well as the contribution of porosity, which controls (lowers) the effective thermal conductivity. Most noticeably, the low peak temperature in this study is a direct result of adding dehydration to the

Table 2: Structure of present day Charon model via different evolution models

Model	H06 ^a	D09 ^b	R14 ^c	MP15 ^d	Section 3 (this study)	Units
Core radius	405	420	430	490	Anhydrous 250	km
					Transition 100	
					Hydrous 135	
Mantle thickness	200	Ice	110	Pure 10	20	
		110		Enriched 35	40	
		Mix	60	Transition 40	25	
		70		Anhydrous 25	35	
Max Temp.	—	1210-1563		1171	912	K
Density	1.757	1.65	1.65	1.63	1.7	g cm ⁻³

^aHussmann *et al.* (2006)

^bDesch *et al.* (2009)

^cRubin *et al.* (2014)

^dMalamud and Prialnik (2015)

model, which serves as a powerful heat sink.

A common conclusion of nearly all models however, is that a near surface outer layer remains unchanged by the evolution. The main difference is in its size, which also depends on how it is defined. If it is defined as the layer overlying fully serpentinized rock, its size in this study is similar to that found by Rubin *et al.* (2014), about 60 km, but if it is defined as containing only fully anhydrous rock, it is approximately half that size, 35 km. If it is defined as retaining precisely the original rock/ice ratio, it is even thinner, approximately 23 km.

4.2 Size Changes During Compaction/Expansion Episodes

In Section 3 we identify, in five evolutionary steps, processes that alter Charon’s size. Our results suggest two contraction-expansion episodes, albeit on different time scales, and for different reasons. The change in radius as a function of time is shown in Fig. 10.

Initially Charon’s radius is much larger than in the present day (since it is assumed to form colder, more porous and with a well-mixed composition). The first contraction episode ($\Delta R = -17.5$ km) corresponds to a period of compaction of warming ice followed by a period of widespread water melting, differentiation and serpentinization of initially

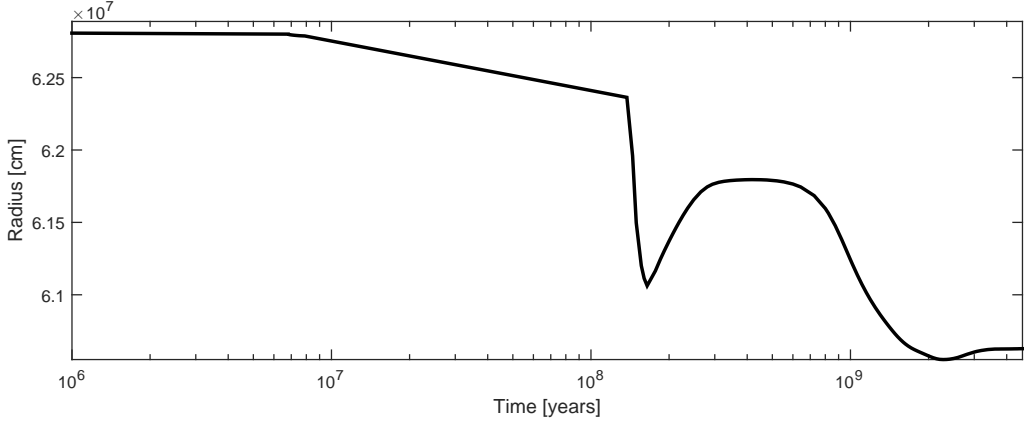


Figure 10: Charon’s radius as a function of time.

pristine anhydrous rock (the water is absorbed in the rock, the net effect being a further decrease in size). Once the rock is fully serpentinized, the remaining water migrates and freezes in the coldest outer parts, forming the mantle. This results in expansion ($\Delta R = 7.4$ km). The second contraction episode ($\Delta R = -12.3$ km) corresponds to the contraction of the rocky core, as increasing temperatures make it more susceptible to compaction. Then the subsequent small expansion ($\Delta R = 0.8$ km) results from water released by dehydration reactions in the rocky core, but it starts only after the peak temperatures in the interior begin to decrease. We postulate that prominent extensional fractures, such as the Serenity Chasma, could be compatible with the first expansion episode. We calculate that the additional surface area resulting from a radius increase of $\Delta R = 7.4$ km would correspond to a 30 km wide fracture, forming a great circle around Charon. The width of Serenity Chasma is 50-60 km between adjacent walls. Nevertheless, Macross Chasma is no more than half that width, and the chasmata network is sporadically connected by much narrower fractures, so that on average (accounting for local variations), this radius increase could be compatible.

The extensional fractures might also have formed around an already existing bulge, as indicated by the high topography walls of Serenity Chasma, as well as in several other locations in the tectonic belt (Fig. 1), including the region around Macross Chasma, or directly below Alice crater. The bulge could have formed by the initial contraction episode

(the outer, cold shell, is at that time only 1/4 its present day thickness, and it deforms to match the reduced volume of the contracting interior), similar to how the equatorial bulge on Iapetus was suggested to have formed (Sandwell and Schubert, 2010; Beuthe, 2010), noting that there are other proposed explanations for Iapetus' equatorial bulge formation (Robuchon *et al.*, 2010; Dombard *et al.*, 2012) that do not involve contraction. In comparison, the second contraction episode involves a thicker mantle, and it deforms on a much longer time scale (several Gyr vs. about 30 Myr), so we might expect less pronounced compressional features. The second expansion episode is even less notable, resulting in a very modest radius increase, so it cannot account for any of the major fractures observed on the surface. Nevertheless, several smaller rille-like features that cut across the moderately cratered plains south of the equator (Stern *et al.*, 2015) are only a few kilometers wide. Although such features do not necessarily form by expansion, it is a possibility.

Other icy bodies have also been observed to undergo global scale contraction/expansion. Titan (Cook-Hallett *et al.*, 2015) and especially Ganymede (Bland and McKinnon, 2015) are good examples, although in their cases, the terrain consists of a very complex, widely spread tectonic patchwork across the surface, very different from what is observed on Charon. There are only two other icy bodies, Iapetus and Tethys, which have localized and specifically oriented surface features that may also be associated with global contraction/expansion. In Iapetus' case, global compression has been one of several explanations suggested for its equatorial bulge (Sandwell and Schubert, 2010; Beuthe, 2010). In Tethys' case, Global expansion has been one of the explanations suggested for Ithaca chasma (Moore *et al.*, 2004), due to freezing of an internal ocean. Unfortunately, it is difficult to compare these objects with Charon, since the evolution of inner solar system icy bodies is contingent upon very different initial, boundary, and external conditions (e.g, different composition, inclusion of various levels of short-lived radiogenic heating, warmer outer layers affected by insolation, the presence of massive parent bodies and/or multiple massive satellites, etc.). Therefore, some hypothesis is required in order to ac-

count for the localization and orientation of Charon’s tectonic belt region, as opposed to being randomly placed and randomly oriented, as one might normally expect.

4.3 Speculation on the Belt’s Localization and Orientation

The model presented in Section 2 is designed to calculate the thermo-physical evolution inside evolving icy objects, however, being 1-dimensional, the model is incapable of explaining localized phenomena. In order to calculate the precise stresses induced by the internal evolution, a very different type of model is required, and therefore it is beyond the scope of this paper. Nevertheless, we suggest two possibilities which can be investigated in future studies, regarding the localization and orientation of the tectonic belt, assuming that it formed as a result of the compressional/extensional environment.

Stern *et al.* (2015) indicate a pronounced surface dichotomy observed between the southern and northern hemispheres of Charon, at least on the Pluto facing side. The south-eastern plains appear significantly smoother than the rougher terrain observed on the north-western side. We point out that the pronounced surface dichotomy on Charon strongly resembles the observed surface dichotomy on Mars (Wilhelms and Squyres, 1984). This structure and its resemblance to the Mars-dichotomy might suggest a similar impact origin as used to explain Mars-dichotomy (Wilhelms and Squyres, 1984; Marinova *et al.*, 2011). The boundary between the rough northern region and the smooth southern regions is complex, and appears to co-align with Charon’s tectonic belt. Here we suggest that these surface features may be linked, and consider two scenarios, both of which include a planetary-scale impact.

equatorial focusing + impact induced rotation axis reorientation.:

In this scenario the tectonic belt formed and localized in a thinner equatorial region, before a subsequent axial reorientation. In that respect we note that though the global tectonic belt is not directly aligned with Charon’s equator, it is close, and the trends of the different chasmata appear parallel, as if to suggest a shift in a primordial equator, of about 20°. Mantle thickness variations around the equator could be produced due to

tidal dissipation during the early tidal despinning (bulge collapse) phase (Beuthe, 2010). They may also result from latitudinal differences in average solar insolation, however this requires a different axial tilt than in the present, for which the average insolation is actually greater in high latitudes (Earle and Binzel, 2015). These thickness variations could then lead to localization of the faults during the contraction/expansion periods around the equatorial region. A later shift in the rotational equator of Charon can be induced by a planetary-scale impact, if the impactor is sufficiently massive (Safronov, 1966), leading to the currently observed configuration. The impact scenario then has the advantage of explaining both Charon's surface dichotomy as well as the orientation of its tectonic belt.

Impact + boundary localization:

In this scenario the order of events is reversed. A massive impact first occurs early-on in the history of Charon, before the formation of its tectonic belt. Such an impact would remove a considerable volume of the outer material, redepositing it on the impact basin periphery. This loss of mass could then be fully compensated by isostatic uplift of unexcavated sub-basin material if enough energy is provided by the impact. Because this material is expected to be denser than the material that was removed, a large depression would remain. The impact provides a natural explanation for why the compressional/extensional features later localized along the complex boundary of the two 'impact hemispheres', instead of randomly. For this sequence of events to make sense, the rolling plains must be older than the tectonic belt, but slightly younger than the Northern hemisphere, so if an accurate determination of their age reveals the opposite, it could provide the means for rejecting this scenario. Thus far an age determination by Stern *et al.* (2015) is inconclusive. In this scenario, the rotational axis could also have changed to the present day orientation as a result of the impact, however this is not explicitly necessary.

5 Conclusions

The main processes that shaped Charon's long-term evolution are presented in Section 3.2. The evolution begins with an initially homogeneous KBO, larger than in the present, and made of a porous mixture of ice and rock. We identify two contraction-expansion episodes in Charon's history, corresponding to various processes in the interior. The present day structure we obtain is complex. The core is made of rock, with a high-density, dehydrated inner part and a more porous outer part, made of hydrated rock. The core is overlain by an ice-rich mantle, some 120 km thick. The mantle is composed of pure ice at its base, the rock fraction variably increasing toward the surface. Only the outermost coldest surface layer might retain the original composition, unaltered by the internal evolution. Compared to previous studies, we obtain a different, more stratified present-day inner structure. We also obtain a much higher rock fraction, due to the inclusion of serpentinization, as well as the contribution of porosity. If zero porosity is assumed, as in most other studies, the rock fraction may only be as high as 55%. Such models advocate a smaller rocky core for Charon than what is possible if porosity is accounted for, as in this study.

Our model shows that Charon has experienced a significant change in radius, both decrease and increase, and that this change could be compatible with the physical appearance of its unique surface features. Our model does not require an early vast ocean, which could also potentially explain the same surface features either by freezing and solidification of the ocean, or by high eccentricity tidally induced fractures requiring an internal liquid layer. These alternative models work only by assuming a warm initial state. In the case of this study, any formation scenario is plausible, and even the in-situ Pluto-Charon binary formation scenario, which would necessarily result in a cold initial state, could be sufficient.

Finally, a hypothesis is required for the localization and specific trend of Charon's tectonic belt. Although we cannot provide a conclusive answer since our model is 1-

dimensional and incapable of investigating localized phenomena, we do offer two speculated possibilities. One is that the compressional/extensional features formed first, focusing around a thinner equatorial region induced by insolation variations or tidal despinning. Then, subsequent to the formation of the belt, Charon's rotational axis shifted to account for the present day orientation. We speculate that this could be the result of a sufficiently massive impact, which could also account for Charon's strange hemispheric surface dichotomy. The second possibility suggests the reversed order of events, that is, an initial impact preceded the formation and localization of the tectonic belt. Later, the belt formed along the boundary of an existing hemispheric dichotomy. This possibility however, is only viable if the impact occurred very early in the history of Charon, the rolling plains being younger than the tectonic belt, which can be verified by age determination.

We conclude with a general prediction, that trans-Neptunian objects of a similar size range should exhibit significant compressional/extensional surface features. If too large (as Pluto), they might relax faster and have a warmer near surface interior. If too small, they might not even have sufficient heat for differentiation and geochemical reactions in the interior. Since variations in the short-lived radiogenic heating and the initial composition are expected to be more moderate in the Kuiper belt, so might we expect less heterogeneity in the surface features of similar sized objects in this region.

6 Acknowledgment

UM and HBP acknowledge support from BSF grant number 2012384, Marie Curie FP7 career integration grant "GRAND", the Minerva center for life under extreme planetary conditions and the ISF I-CORE grant 1829/12. We would also like to thank Erez Michaeli for providing assistance in using the MESA stellar evolution code, as well as other helpful discussions.

References

- Barr, A. C., and G. C. Collins 2015. Tectonic activity on pluto after the charon-forming impact. *Icarus* **246**, 146–155.
- Beuthe, M. 2010. East-west faults due to planetary contraction. *Icarus* **209**, 795–817.
- Bland, M. T., and W. B. McKinnon 2015. Forming ganymede’s grooves at smaller strain: Toward a self-consistent local and global strain history for ganymede. *Icarus* **245**, 247–262.
- Brozović, M., M. R. Showalter, R. A. Jacobson, and M. W. Buie 2015. The orbits and masses of satellites of pluto. *Icarus* **246**, 317–329.
- Buie, M. W., W. M. Grundy, E. F. Young, L. A. Young, and S. A. Stern 2006. Orbits and photometry of pluto’s satellites: Charon, s/2005 p1, and s/2005 p2. *The Astronomical Journal* **132**, 290–298.
- Canup, R. M. 2005. A giant impact origin of pluto-charon. *Science* **307**, 546–550.
- Cheng, W. H., M. H. Lee, and S. J. Peale 2014. Complete tidal evolution of pluto-charon. *Icarus* **233**, 242–258.
- Cook-Hallett, C., J. W. Barnes, S. A. Kattenhorn, T. Hurford, J. Radebaugh, B. Stiles, and M. Beuthe 2015. Global contraction/expansion and polar lithospheric thinning on titan from patterns of tectonism. *Journal of Geophysical Research (Planets)* **120**, 1220–1236.
- Desch, S. J., J. C. Cook, T. C. Doggett, and S. B. Porter 2009. Thermal evolution of kuiper belt objects, with implications for cryovolcanism. *Icarus* **202**, 694–714.
- Dombard, A. J., A. F. Cheng, W. B. McKinnon, and J. P. Kay 2012. Delayed formation of the equatorial ridge on iapetus from a subsatellite created in a giant impact. *Journal of Geophysical Research (Planets)* **117**, 3002.

- Earle, A. M., and R. P. Binzel 2015. Pluto's insolation history: Latitudinal variations and effects on atmospheric pressure. *Icarus* **250**, 405–412.
- Hussmann, H., F. Sohl, and T. Spohn 2006. Subsurface oceans and deep interiors of medium-sized outer planet satellites and large trans-neptunian objects. *Icarus* **185**, 258–273.
- Kenyon, S. J., and B. C. Bromley 2012. Coagulation calculations of icy planet formation at 15-150 au: A correlation between the maximum radius and the slope of the size distribution for trans-neptunian objects. *The Astronomical Journal* **143**, 63.
- Malamud, U., and D. Prialnik 2013. Modeling serpentinization: Applied to the early evolution of enceladus and mimas. *Icarus* **225**, 763–774.
- Malamud, U., and D. Prialnik 2015. Modeling kuiper belt objects charon, orcus and salacia by means of a new equation of state for porous icy bodies. *Icarus* **246**, 21–36.
- Malamud, U., and D. Prialnik 2016. A 1-d evolutionary model for icy satellites, applied to enceladus. *Icarus* **268**, 1–11.
- Marinova, M. M., O. Aharonson, and E. Asphaug 2011. Geophysical consequences of planetary-scale impacts into a mars-like planet. *Icarus* **211**, 960–985.
- Moore, J. M., P. M. Schenk, L. S. Bruesch, E. Asphaug, and W. B. McKinnon 2004. Large impact features on middle-sized icy satellites. *Icarus* **171**, 421–443.
- Nesvorný, D., A. N. Youdin, and D. C. Richardson 2010. Formation of kuiper belt binaries by gravitational collapse. *The Astronomical Journal* **140**, 785–793.
- Paxton, B., L. Bildsten, A. Dotter, F. Herwig, P. Lesaffre, and F. Timmes 2011. Modules for experiments in stellar astrophysics (mesa). *The Astrophysical Journal Supplement* **192**, 3.
- Pires dos Santos, P. M., A. Morbidelli, and D. Nesvorný 2012. Dynamical capture in the pluto-charon system. *Celestial Mechanics and Dynamical Astronomy* **114**, 341–352.

- Prialnik, D., and R. Merk 2008. Growth and evolution of small porous icy bodies with an adaptive-grid thermal evolution code. i. application to kuiper belt objects and encedadus. *Icarus* **197**, 211–220.
- Rhoden, A. R., W. Henning, T. A. Hurford, and D. P. Hamilton 2015. The interior and orbital evolution of charon as preserved in its geologic record. *Icarus* **246**, 11–20.
- Robuchon, G., G. Choblet, G. Tobie, O. Čadek, C. Sotin, and O. Grasset 2010. Coupling of thermal evolution and despinning of early iapetus. *Icarus* **207**, 959–971.
- Rubin, M. E., S. J. Desch, and M. Neveu 2014. The effect of rayleigh-taylor instabilities on the thickness of undifferentiated crust on kuiper belt objects. *Icarus* **236**, 122–135.
- Safronov, V. S. 1966. Sizes of the largest bodies falling onto the planets during their formation. *Soviet Astronomy* **9**, 987–991.
- Sandwell, D., and G. Schubert 2010. A contraction model for the flattening and equatorial ridge of iapetus. *Icarus* **210**, 817–822.
- Stern, S. A., et al. 2015. The pluto system: Initial results from its exploration by new horizons. *Science* **350**(6258).
- Stern, S. A., H. A. Weaver, A. J. Steffl, M. J. Mutchler, W. J. Merline, M. W. Buie, E. F. Young, L. A. Young, and J. R. Spencer 2006. A giant impact origin for pluto’s small moons and satellite multiplicity in the kuiper belt. *Nature* **439**, 946–948.
- Ward, W. R., and R. M. Canup 2006. Forced resonant migration of pluto’s outer satellites by charon. *Science* **313**, 1107–1109.
- Wilhelms, D. E., and S. W. Squyres 1984. The martian hemispheric dichotomy may be due to a giant impact. *Nature* **309**, 138–140.
- Williams, D. M., and D. Pollard 2002. Earth-like worlds on eccentric orbits: excursions beyond the habitable zone. *International Journal of Astrobiology* **1**, 61–69.